The final publication is available at

http://doi.org/10.1002/cssc.201800420

Additional Information

Mixed ionic-electronic conduction in $NiFe_2O_4$ – $Ce_{0.8}Gd_{0.2}O_{2-\delta}$ nanocomposite thin films for oxygen separation

Cecilia Solís[1], Fidel Toldra-Reig[1], María Balaguer[1], Simona Somacescu[2], Julio Garcia-Fayos[1], Elena Palafox[1], José M. Serra[1]

[1] *Instituto de Tecnología Química (Universitat Politècnica de València - Consejo Superior de Investigaciones Científicas), Avenida de los Naranjos s/n.46022 Valencia, Spain*

[2] *"Ilie Murgulescu" Institute of Physical Chemistry, Romanian Academy, Spl. Independentei 202, 060021, Bucharest, Romania*

Abstract

$NiFe_2O_4$ - $Ce_{0.8}Gd_{0.2}O_{2-\delta}$ (NFO/CGO) nanocomposite thin films were prepared by simultaneously r.f. magnetron sputtering of both, NFO and CGO, ceramic targets. The aim is the growth of CO_2 stable composite layers that combine the electronic and ionic conduction of the separate NFO and the CGO phases for oxygen separation applications. The effect of the deposition temperature on the films microstructure was studied in order to obtain high quality composite thin films. The ratio of both phases was changed by applying different power to each ceramic target. The amount of each deposited phase as well as the different oxidation states of the nanocomposite constituents was analyzed by means of XPS. The transport properties were studied by total conductivity measurements as a function of temperature and pO_2. These analyses enabled to (1) select the best deposition temperature (400 ºC), (2) correlate the *p*-type electronic behavior of the NFO phase with the hole hopping between Ni^{3+} - Ni^{2+} and (3) follow the conductivity behaviour of the grown composite layer (prevailing ionic or electronic character) attained by varying the amount of each phase. The nanocomposite sputtered layer exhibited high ambipolar conduction and surface exchange activity. A 150 nm-thick nano-grained composite thin film was deposited on a 20 µm-thick BSCF asymmetric membrane, obtaining up to 3.8 ml·min^{-1}·cm^{-2} O_2 at 1000 ºC under full CO_2 atmosphere.

Keywords: ceria; nanocomposite; Ionic conductor; sputtering; oxygen membrane

1. Introduction

The use of O_2 rich gas streams in several industrial processes is receiving a lot of attention, mainly due to the gain in sustainability and process efficiency. One of the most considered applications is oxyfuel technology, consisting of burning of a fuel with pure O_2, thus allowing more efficient combustion processes, minimizing NO_x formation, and the direct CO_2 sequestration. [1] Nowadays, O_2 is mostly produced by highly energy-demanding and costly cryogenic air separation units and pressure-swing absorption. [2]. Oxygen transport membranes (OTMs) are a promising alternative technology that can be integrated in the industrial processes for on-site O_2 production for medium and small-scale applications instead traditional methods [3] [4]

OTMs consist of mixed ionic and electronic conductivity (MIEC) materials that allow the diffusion of O^{2-} (driven by an oxygen partial pressure gradient across the membrane) and electronic carriers in the opposite direction for charge compensation, obtaining a net O_2 separation with infinite selectivity. Permeation of O_2 when bulk diffusion is limiting is described by Wagner's equation[1], which determines that OTMs performance is affected by: (i) the ambipolar conductivity of the constituent material (σ_{amb}), (ii) the membrane thickness (L), and (iii) the membrane operation conditions (pO_2 gradient, temperature and atmosphere). Perovskite-type (ABO_3) membranes -and in particular $Ba_{0.5}Sr_{0.5}Co_{0.8}Fe_{0.2}O_{3-\delta}$ (BSCF)- exhibit the highest $J(O_2)$ due to their high MIEC, although they are not stable in the harsh conditions that can be encountered in reactors and combustors (as CO_2, H_2O, SO_2 presence in the gas streams). A trade-off between good ionic and electronic conductivity and stability may be achieved by combining the best characteristics of different materials in a composite. These composites consist of (1) an electron conducting material, which allows the percolation of electrons, and (2) an ionic conductor that transports the O^{2-} through the membrane. The ceramic-ceramic (cercer) dual-phase compounds[5] have been proposed as an economically attractive solution regarding composite OTMs. Several crystalline structures have been combined, demonstrating stability of both phases against reaction and

---

[1] $J(O_2) = \frac{RT}{16F^2L} \int_{pO_2''}^{pO_2'} \sigma_{amb}(pO_2) dlnpO_2$, where $J(O_2)$ is the O_2 permeation flux in mol·m⁻²·s⁻¹, R is the gas constant, F is the Faraday constant, L is the membrane thickness, σ_{amb} is the ambipolar conductivity ($\sigma_{amb} = \frac{\sigma_e \cdot \sigma_i}{\sigma_e + \sigma_i}$, where σ_i is the ionic and σ_e the electronic conductivities, respectively), and pO_2' and pO_2'' are the O_2 partial pressures at the high pressure side and low pressure side, respectively.

the compatibility of their thermal expansion coefficients (TEC) in order to produce mechanically resistant membranes, e.g. fluorites, perovskites, spinels and rock salts.[6] While materials with perovskite and spinel structure are used as electronic conducting phase,[7] fluorite materials constitute the oxygen conductor phase with high chemical stability.[8]. In this way, different doped ceria fluorites and several spinel composite membranes have shown promising CO_2 stable permeation properties.[9]

In particular, $NiFe_2O_4$ (NFO) and $Ce_{0.9}Gd_{0.1}O_{2-\delta}$ (CGO10) were reported to be stable upon heating and cooling cycling between room temperature and 1000 °C in air and in an atmosphere with 50 vol % CO_2 and 50 vol % N_2. [10]The thermal expansion coefficient (TECs) difference of both structures (10.3×10^{-6} K^{-1} of NFO and 11.9×10^{-6} K^{-1} of CGO10)[8a, 11] is within acceptable limits to the materials compatibility (15–25%).[12] At 1000 °C, $J(O_2)$ of 0.31 and 0.27 ml·min^{-1}·cm^{-2} were obtained on a 0.5 mm thick membrane for the sweep gases He and CO_2, respectively. [10] For industrial applications, a minimum of 3.5 ml·min^{-1}·cm^{-2} oxygen rate is required. [13] Following Wagner equation predictions, the $J(O_2)$ can be increased by decreasing membrane thickness (*L*) as long as O_2 transport is controlled by bulk diffusion, occurring above the critical length (L_c), characteristic of each material. [14] Hence, different methods to decrease the thickness of a dense membrane layer have been proposed e.g. screen printing, [15] tape casting [16], spray pyrolysis[17] or r.f. magnetron sputtering [18], for thinner layers.

Sputtering is a versatile method to produce thin films over a large area with a high uniformity. By optimizing the film, the properties of the layer can be tuned in terms of electrical transport or mechanical properties by adjusting the deposition parameters. For example, mechanical properties can be modified by controlling thin film thickness [19] or fixing preferential orientation by selecting the substrate temperature [20]. In addition, several targets can be co-sputtered at the same time giving the possibility of synthesize materials with a post-treatment, [21] or forming composites[22].

This work is focused on the study of thin films of composites made of NFO spinel and $Ce_{0.8}Gd_{0.2}O_{2-\delta}$ (CGO) fluorite as electronic and ionic conducting phases, respectively, motivated by the high stability against CO_2 showed by both NFO and CGO structures.[8a, 8b, 10] The deposition of the cercer thin films was done by co-sputtering simultaneously NFO and CGO targets.[18] Different deposition temperatures, atmospheres and r.f. power were

3

used for the thin film optimization, which was based on a thorough analysis of the thin films microstructure and their transport properties at high temperature. The transport properties were studied by DC conductivity and electrical conductivity relaxation, and correlated to the thin film characteristics, measured by XRD, FESEM, XPS, and AFM. Finally, composite permeation properties were tested by using an optimized thin film composite on a 20 μm BSCF asymmetric membrane, combining the high permeation flux of the BSCF and the stability properties of the NFO/CGO composite.

2. Experimental Section

$Ce_{0.8}Gd_{0.2}O_{2-\delta}$ (CGO) powder was purchased from Treibacher Industrie AG, while $NiFe_2O_4$ (NFO) powder was prepared by Pechini method.[9d] One inch ceramic targets were prepared by uniaxially pressing into pellets at (59.2 MPa) for 3 minutes and subsequently sintering in air at 1400 ºC for 5 h. X-ray diffraction (XRD) of the sintered targets confirmed the complete formation of the corresponding fluorite and spinel structures, respectively.[11, 23] The thin films were deposited with a Pfeiffer Classic 250 deposition system equipped with two radiofrequency (13.56 MHz) sources. One inch $NiFe_2O_4$ and $Ce_{0.8}Gd_{0.2}O_{2-\delta}$ ceramic targets were used for sputtering of single films of each material and co-sputtering the cercer nanocomposite on a rotating substrate holder, with r.f. powers ranging from 8 to 25 W. The base pressure of the chamber before the deposition was 2×10^{-6} mbar or lower. The working pressure was 2.9×10^{-2} mbar with mixed argon-oxygen gas ratio 10/2. The distance target-substrate was kept to 5 cm and the substrate temperature was changed from room temperature (RT) up to 600 ºC. Different thicknesses were deposited and controlled by deposition duration. All samples were deposited on Si (100) and amorphous quartz substrates in order to perform different characterizations.

The crystal structure of the films was checked by XRD measurements carried out by a PANalytical Cubix fast diffractometer, using $CuK_{\alpha1,2}$ radiation and an X'Celerator detector in Bragg-Brentano geometry.

The surface morphology of the films and the fracture cross sections were observed by ZEISS Ultra55 field emission scanning electron microscope (FESEM). The thickness of the films was determined from the fracture cross section FESEM images, preferably with

samples deposited on Si. The topography and roughness of the thin layers was measured by a Bruker Multimode 8 contact atomic force microscope (AFM).

The planar electrical conductivity of the films was measured by standard four-point DC technique, on films deposited on quartz substrates, by using silver wires and paste for contacting. Measurements were recorded as the temperature decreases from 800 to 400 ºC at 1 ºC/min at a constant atmosphere, in different oxygen partial pressures (pO_2).[8a]

The electrical conductivity relaxation technique (ECR) was carried out in a tubular oven in which the gas volume was minimized in order to achieve an almost instantaneous pO_2 change. Experiments were performed by measuring the impedance at a fixed frequency of 100 Hz with a Phase Sensitive Multimeter 1735 with an IAI interface from Newtons 4th Ltd.[8b, 24] The oxygen exchange kinetics was investigated by alternatively swapping oxygen partial pressure from 1 to 0.21 atm at some given temperatures. In this case, as we are measuring thin films, the relaxation is rate limited by the surface reaction, k, and values can be extracted from fittings to the ECR curves to equation (1):

$$g(t) = \frac{\sigma(t) - \sigma_0}{\sigma_\infty - \sigma_0} = 1 - A\exp\left(-\frac{t}{\tau}\right)$$

(1)

with $\tau = \dfrac{l}{k}$, where l is the thickness of the film.[8b, 25]

Oxygen permeation studies were carried out in a lab-scale quartz reactor. The asymmetric membranes where the thin films were deposited were supplied by Forschungszentrum Jülich. The membranes consisted of all-$Ba_{0.5}Sr_{0.5}Co_{0.8}Fe_{0.2}O_{3-\delta}$ asymmetric membrane comprising a 20 μm-thick dense layer supported on a 750 μm-thick BSCF porous substrate. Synthetic air (21%, vol. O_2 in the feed stream) was fed into the oxygen-rich chamber, while argon and CO_2 mixtures were used as sweep gases on the permeate side in a 4-end mode configuration. Both streams were fed at atmospheric pressure. All streams were individually mass flow controlled. The temperature was measured by a thermocouple attached close to the membrane. A PID controller maintained temperature variations within 2 ºC of the set point. Membrane gas leak-free conditions were achieved using gold rings. The permeate was analyzed at steady state by online gas chromatography using a micro-GC Varian CP-4900 equipped with Molsieve5A, Pora-Plot-Q glass capillary, and CP-Sil modules. Membrane gas leak-free conditions were ensured by continuously monitoring the

nitrogen concentration in the product gas stream. An acceptable sealing was achieved when the ratio between the oxygen flow leak and the oxygen flux was lower than 3%. The data reported here were achieved at steady state after 1 h in the reaction stream. Each test was repeated three times to minimize the analysis error. The experimental analytical error was below 0.5%.

Surface analysis performed by X-ray photoelectron spectroscopy (XPS) was carried out on PHI Quantera equipment with a base pressure in the analysis chamber of 10^{-9} mbar. The X-ray source was monochromatic Al Kα radiation (1486.6 eV) and the overall energy resolution is estimated at 0.65 eV by the full width at half-maximum (FWHM) of the Au4f7/2 photoelectron line (84 eV). The charging effect was minimized by using a dual beam (electrons and Ar ions) as neutralizer while the spectra were calibrated using the C1s line (BE = 284.8 eV) of the adsorbed hydrocarbon on the sample surface (C-C and/or (CH)n bondings). As this spectrum was recorded at the start and at the end of each experiment the energy calibration during experiments was reliable. For in depth analysis, the incidence angle of the ion beam was 45º and the sputter rate was ~2.5 nm/min

3. Results and discussion

Prior to NFO-CGO thin film deposition by co-sputtering, the deposition of each material was studied independently. NFO thin film deposition was optimized in a previous work[18] and the obtained films show a structure that matches that of the reported NFO bulk cubic spinel.[11] NFO films show predominant *p*-type electronic conductivity in contrast to the *n*-type electronic behaviour reported for the bulk. This difference is assigned to the higher amount of Ni^{3+} in the films due to the creation of cation vacancies in the ferrite lattice, that produce the hole hopping between Ni^{3+} - Ni^{2+}.[26] The Ni^{3+}/Ni^{2+} ratio was measured by XPS, which corroborates that the films have double ratio (0.42) than the bulk.[18]

Similar conditions as in the case of NFO thin films were selected for the CGO films deposition. As deposited, the film grown at RT is amorphous, deduced from the absence of any diffraction peaks. When the deposition temperature is increased, the crystallization of the CGO films is produced and the obtained films show different preferential orientations depending on the deposition temperature.

NFO/CGO composite films were grown by co-sputtering process of NFO and CGO simultaneously. The amount of the different phases was firstly estimated from the deposition rate of each material (NFO/CGO 25/75 vol.%) and afterwards calculated from XPS analysis. Figure 1a shows the XRD patterns of the as deposited at RT, 400 and 600 ºC NFO/CGO composite films. The composite grown at RT is predominantly amorphous, as expected from the identical behaviour of NFO and CGO single films and ascribed to the very low energy applied for the deposition, which was not sufficient for the crystal formation. At higher temperatures, 400 and 600 ºC, conditions at which both materials have shown enough energy for crystallization, obtained XRD patterns only show intensive peaks corresponding to the CGO while NFO peaks show very low intensity. Furthermore, as in the case of the single CGO films, CGO phase shows preferential (111) and (200) orientation for depositions at 400 and 600 ºC, respectively. These temperature dependent texture orientations were previously reported for other CGO and CeO_2 thin films, although no unified explanation exists from theoretical and experimental points of view.[27] After thin film annealing at 800 ºC for 2 h shown in Figure 1b, the pattern peaks are narrower, as corresponds to the grain growth with temperature, the CGO preferential orientation remains and the NFO phase is better defined, although its intensity is much lower than that of CGO due to the lower amount of this phase, as expected from the deposition rate of each material.
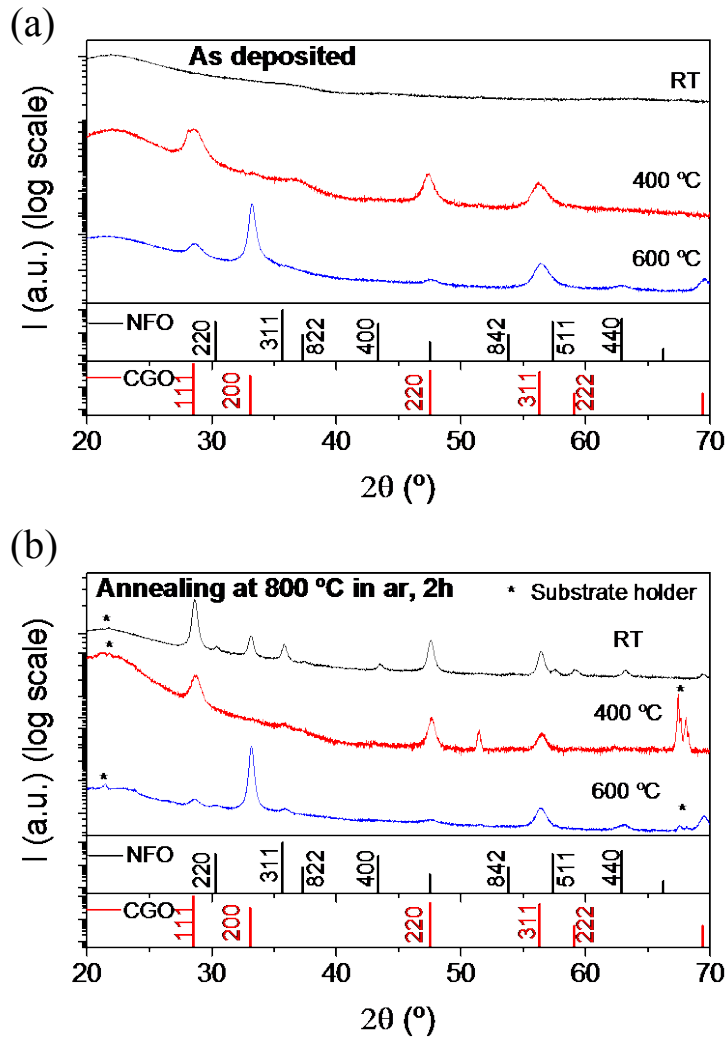
Figure 1: XRD patterns of three different NFO/CGO composite films deposited at RT, 400 and 800 ºC (a) as grown and (b) after annealing in air for 2 hour at 800 ºC. NFO and CGO reference patterns are also showed for comparison. r.f. 25/25 W

The surface morphology of the aforementioned NFO/CGO composite films is depicted in Figure 2. FESEM analysis reveals dense, homogenous and crack-free surfaces at the different deposition temperatures (Figure 2a, b and c) and after the annealing process at 800 ºC in air for 2 h (d, e and f, respectively). Although the grain size growth caused by the thermal treatment is evident (also from XRD analysis), the small grain size of both components does not allow a clear distinction between NFO and CGO grains. The corresponding cross-section images of each annealed sample are also showed in the insets of Figure 2. Furthermore, there is a thickness difference that corresponds to distinct deposition time. An electron backscatter diffraction (EBSD) analysis was performed to

identify both crystalline phases, but no signal could be detected to the limit of the technique and due to the small diffraction domains inside the particles.
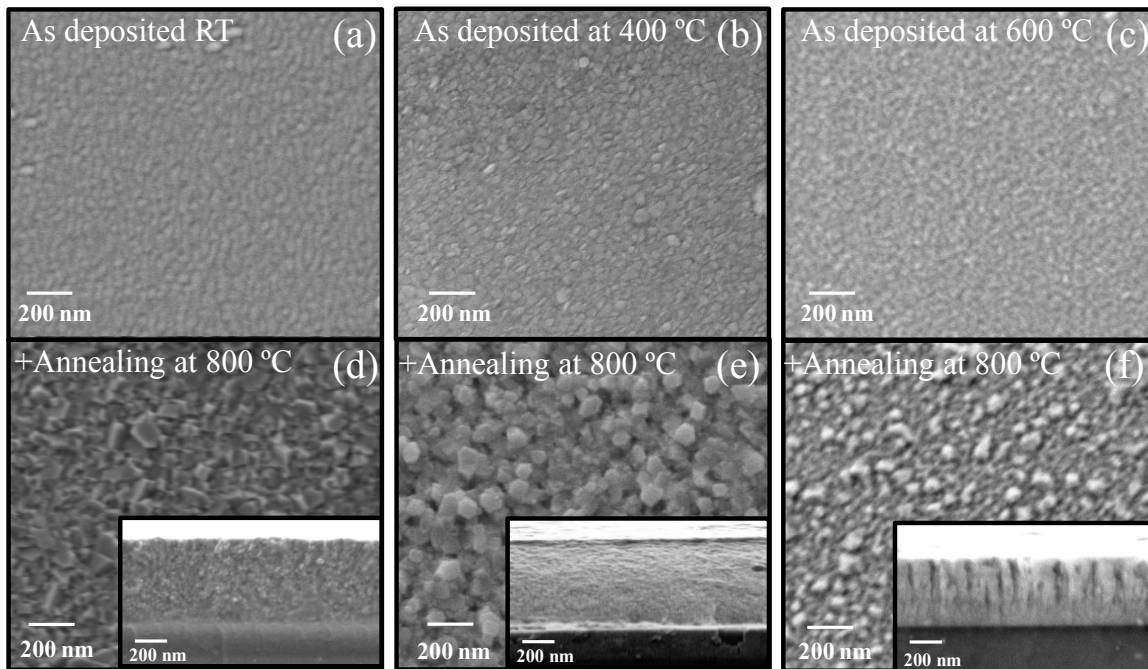

Figure 2: FESEM images of different composite films deposited at RT (a), 400 ℃ (b) and 800 ℃ (d) and after annealing in air for 2 h at 800 ℃ (d), (e) and (f), respectively. r.f. 25/25 W. Note that the image of the as-deposited sample at 400 ℃ was taken after 3 s Pt sputter deposition.

The microstructure after the annealing at 800 ℃ of the thin film deposited at 400 ℃ was studied more in detail by means the AFM and SEM analysis (Figure 3). The thin films are smooth, with surface roughness of Ra ≈ 7 nm. AFM and SEM images reveal the presence of two different phases, one with bigger grains (up to 100 nm) than the other one. Although it was not possible to determine by EDX which phase corresponds to which microstructure (due to the very small grain size) the images present a good distribution of both of them. In fact, the apparent connection between grains of the same phase will be translated into continuous electronic and ionic pathways for ambipolar oxygen transport, respectively, as it is later checked. Considering the grain morphology, polyhedral shapes are typically obtained for NFO with respect to CGO that tends to form globular grains.
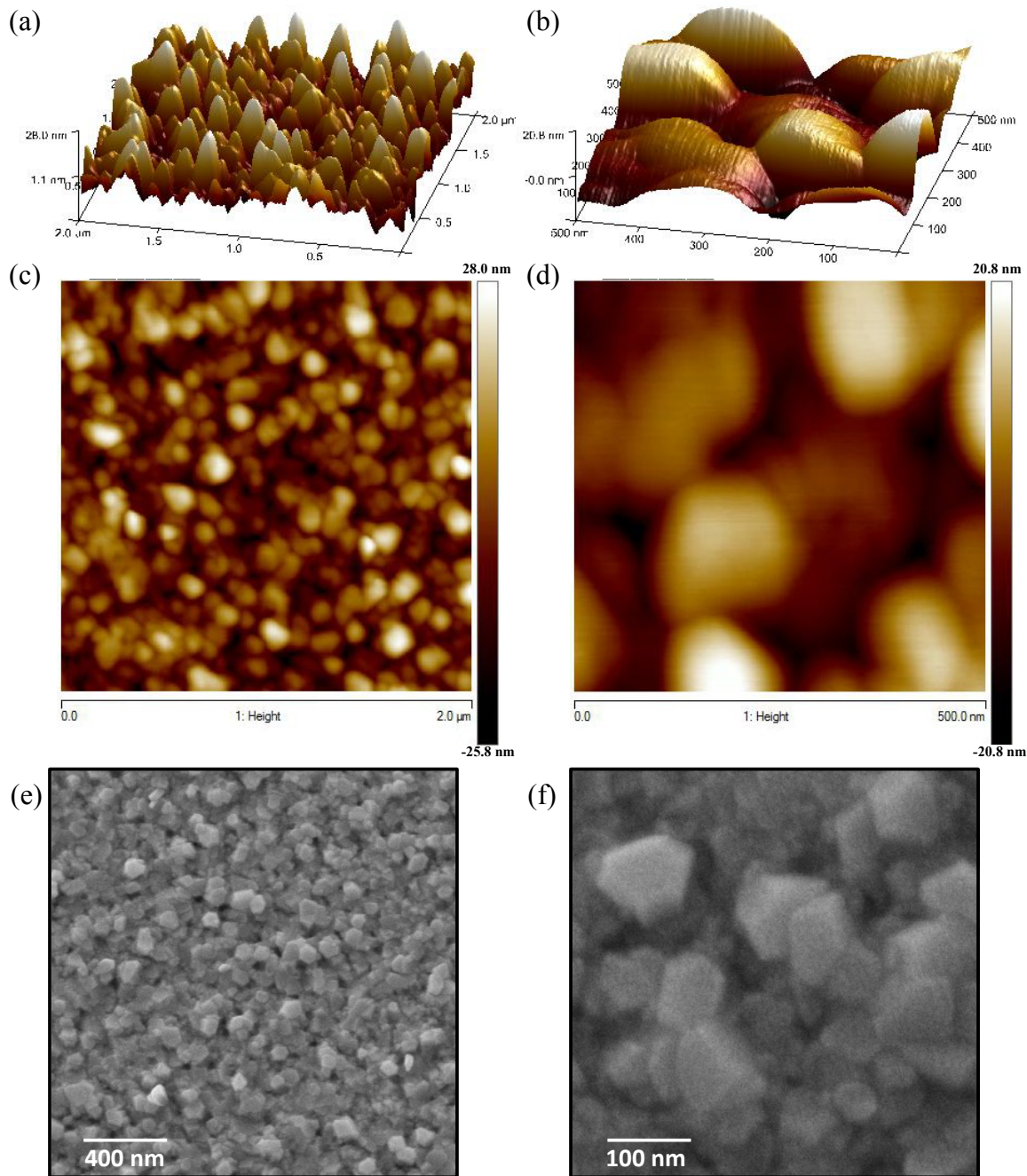
Figure 3: 3D (a) and (b) and 2D (c) and (d) AFM images at two different magnifications, and SEM images at the same magnifications (e) and (f) of the composite film deposited at 400 ºC after the annealing at 800 ºC

The composition ratios NFO/CGO, and oxidation states of the composite constituent elements of thin films sputtered under different conditions were analyzed by XPS. Ni2p3/2 XPS spectra is depicted in Figure 7a, b and c. The Ni^{3+}/Ni^{2+} ratio was calculated from the deconvolution of the spectra, obtaining values of 0.49, 0.39 and 0.54 for the samples

deposited at RT, 400 and 600 ºC, respectively. The estimated errors related to these values are in the range of ±5%. These values are closer to the 0.5 ratio observed in the NFO thin films with regard to the 0.16 ratio observed in NFO bulk material, which has shown to have an impact on the electronic conductivity behaviour.[18]
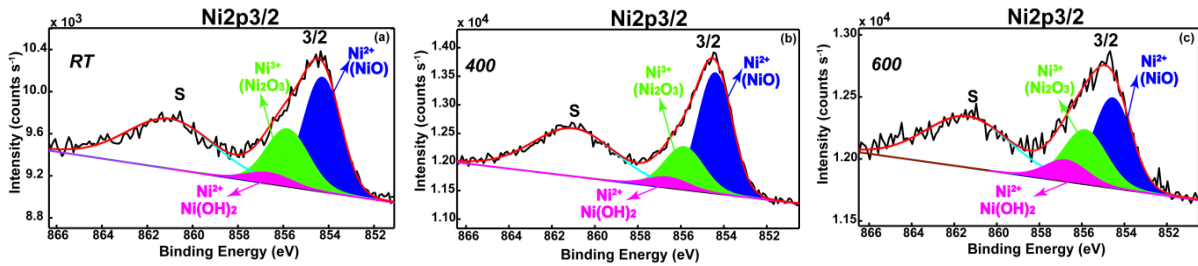

Figure 4: Ni2p3/2 XPS deconvoluted spectra in the "as received" (surface) stage for NFO-CGO films deposited at RT (a), 400 (b) and 600 ºC (c)

Table 1 summarizes the XPS results for the films sputtered at different temperatures. The spectra were recorded in the as-received state to avoid any sputter induced changes in the oxidation states. Indeed, the sensitivity of ceria to Ar ion etching is well known even under very gentle setup conditions. Iron surface chemistry (Supplementary information Figure S1b, e, h) shows the features of a mixture of 3+ and 2+ oxidation states evidenced by both the 2p3/2 binding energies and the shape of the spectra (the presence of satellites). The sample deposited at 600 ºC shows the highest percentage of Fe^{3+} on the as-received surface while the samples deposited at RT and 400 ºC display a lower content of this oxidation state. O1s deconvoluted spectra (Figure S1a, d and g) show three features assigned to oxygen bonded in the lattice (O^{2-}), OH groups and H_2O adsorbed on the top of the surface layer (see Table 1). Ce3d and Ce4d photoelectron spectra (Figure S1c and f) are typical spectral fingerprint for 4+ oxidation state. It is worth to mention that the Ce^{4+} valence state is not affected by the used deposition method. Previous reports highlighted the presence of Ce^{3+} on thin films, as a result of the different parameters used in similar sputtering deposition method.[28] This conclusion can be drawn from both Ce3d and Ce4d characteristic spectra as compared to the reference spectrum presented in the Supplementary information, Figure S2. Finally, Gd3d5/2 lines (showed in Supplementary information, Figure S1 i) are characteristic of Gd^{3+}, assignment strengthen by recording

Gd4d spectrum (Figure S1 f) as well as our own reference sample (see Supplementary information, Figure S3).

Table 1: Binding energies (BEs) of the most prominent XPS transitions (C1s, O1s, Ni2p3/2, Fe2p and Gd3d5/2)

Sample	Binding energy (eV)				
	C1s	**O1s**	**Ni2p3/2**	**Fe2p**	**Gd3d5/2**
RT .	284.8	529.4 (O^{2-}) 531.6 (OH) 532.7 (H_2O)	854.4 (Ni^{2+}/NiO) 855.8 (Ni^{3+}/Ni_2O_3) 856.3 (Ni^{2+}/Ni(OH)$_2$)	710.6	1187.0
400	284.8	529.5(O^{2-}) 531.4(OH) 532.9(H_2O)	854.3 (Ni^{2+}/NiO) 855.8 (Ni^{3+}/Ni_2O_3) 856.4 (Ni^{2+}/Ni(OH)$_2$)	710.6	1187.1
600	284.8	530.1(O^{2-}) 531.5(OH) 533.0(H_2O)	854.5 (Ni^{2+}/NiO) 855.8 (Ni^{3+}/Ni_2O_3) 856.6 (Ni^{2+}/Ni(OH)$_2$)	710.9	1186.8
CGO target	284.8	528.7(O^{2-}) 531.4(OH)	-	-	1186.7
CGO thin film	284.8	528.5(O^{2-}) 531.6(OH)	-	-	1186.6
NFO target	284.8	529.9(O^{2-}) 531.5(OH) 532.9 (H_2O)	854.7 (Ni^{2+}/NiO) 855.9 (Ni^{3+}/Ni_2O_3)	710.7	-
NFO film	284.8	530.0(O^{2-}) 531.5(OH) 532.8 (H_2O)	854.6 (Ni^{2+}/NiO) 855.9 (Ni^{3+}/Ni_2O_3)	710.8	-

The NFO/CGO ratio of both phases was calculated from XPS analysis (XPS depth profiles shown in Supporting Figure S4). In depth profile of the XPS spectra (Figure 8a-c) show that there is a carbon layer (likely from adsorbed hydrocarbons) confined on a few surface monolayers, especially on the samples deposited at 400 and 600 ºC (~35 atom %). The phases buried under this deposit were detected after removal of this contaminant layer (1

min Ar ion etching). The profiles of the atom relative concentrations (atom%) are very similar for the samples deposited at RT and 600 ºC, but differ from that corresponding to the sample deposited at 400 ºC. While samples deposited at RT and 600 ºC exhibit a homogeneous in-depth composition, the sample deposited at 400 ºC shows an inhomogeneous in-depth phase distribution in the first layers. Therefore, the NFO/CGO (wt.%) ratios were calculated from the experimentally obtained concentrations after 12 min Ar ion etching (~ 35 nm), since the transport properties are related mainly to the *bulk* phase of our films (> 30 nm) rather than the outermost surface layer (< 2 nm). Thus, the obtained NFO/CGO (wt.%) values were 0.27, 0.17 and 0.24 for the samples deposited at RT, 400 and 600 ºC, respectively.
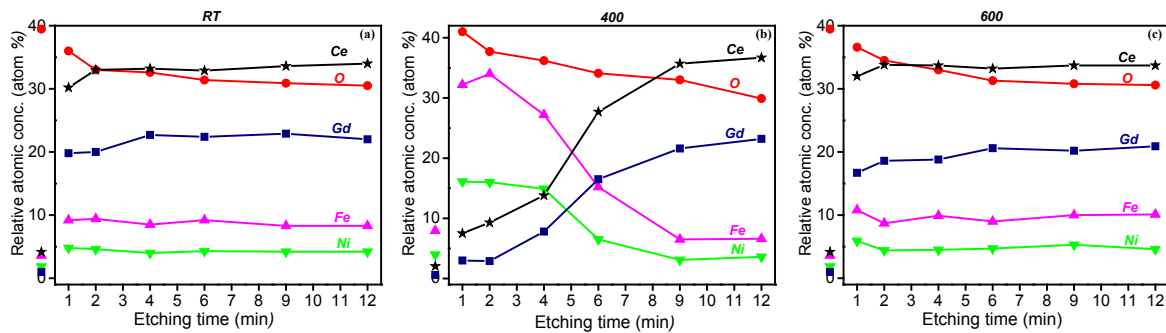

Figure 5: The related in-depth relative concentrations determined from the corresponding XPS spectra (a) at RT; (b) at 400ºC; and (c) at 600ºC)[29]

The impact of the microstructural characterization and surface of the thin films on the electrochemical transport properties of the sputtered layers was studied. The thermal behaviour of total conductivity of the NFO/CGO composites (Figure 4) is compared with grown NFO and CGO thin films and the bulk composite material. The conductivity of the composite films follows a similar Arrhenius behaviour than NFO, i.e. similar activation energy. The grown CGO films exhibits higher activation energy. The total conductivity of the thin films is lower than that reached by the NFO/CGO 60/40 bulk sample, while it is in between conductivity values of the NFO and the CGO thin films, closer to the latter due to the higher amount of this phase in the composite (~1/6). The nanocomposite thin films deposited at 400 and 600 ºC show slightly smaller conductivity than that of the film deposited at RT, attributed to differences in the film microstructure (Figure 2).
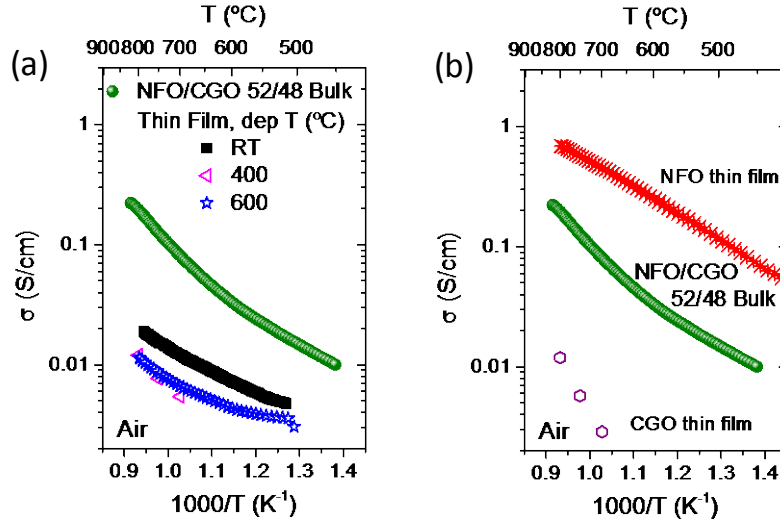
Figure 6: Total conductivity in air as a function of inverse temperature (a) of different cercer thin films and (b) of reference CGO and NFO thin films. Data of the NFO/CGO 52/48 bulk material is also plotted for comparison in both graphs

pO_2 dependence of the conductivity at 700 ºC of the different thin films and bulk reference material is shown in Figure 6. The behaviour of the thin films substantially differs from the bulk material. Namely, the bulk material (NFO/CGO 52/48 wt.) shows a slope close to -1/4, characteristic of a predominant *n*-type electronic conductor, while the film (NFO/CGO 1/6) show positive slopes of around 0.1-0.2. This slope for the composite film arises from an averaged (or additive) behaviour of both constituents, NFO and CGO films. Specifically, CGO film shows a nearly zero slope as expected from a pure ionic conductor while NFO film shows a ¼ slope, as corresponds to a predominant *p*-type electronic conductor. This is in contrast to the bulk material, which exhibits a -1/4 slope typical of *n*-type electronic conductors.[18] The particular *n*-type electronic conductivity of the NFO thin film is ascribed to the electron hopping between Fe^{3+} - Fe^{2+}, while the NFO *p*-type conductivity is ascribed to the hole hopping between Ni^{3+} - Ni^{2+}.[26, 30]
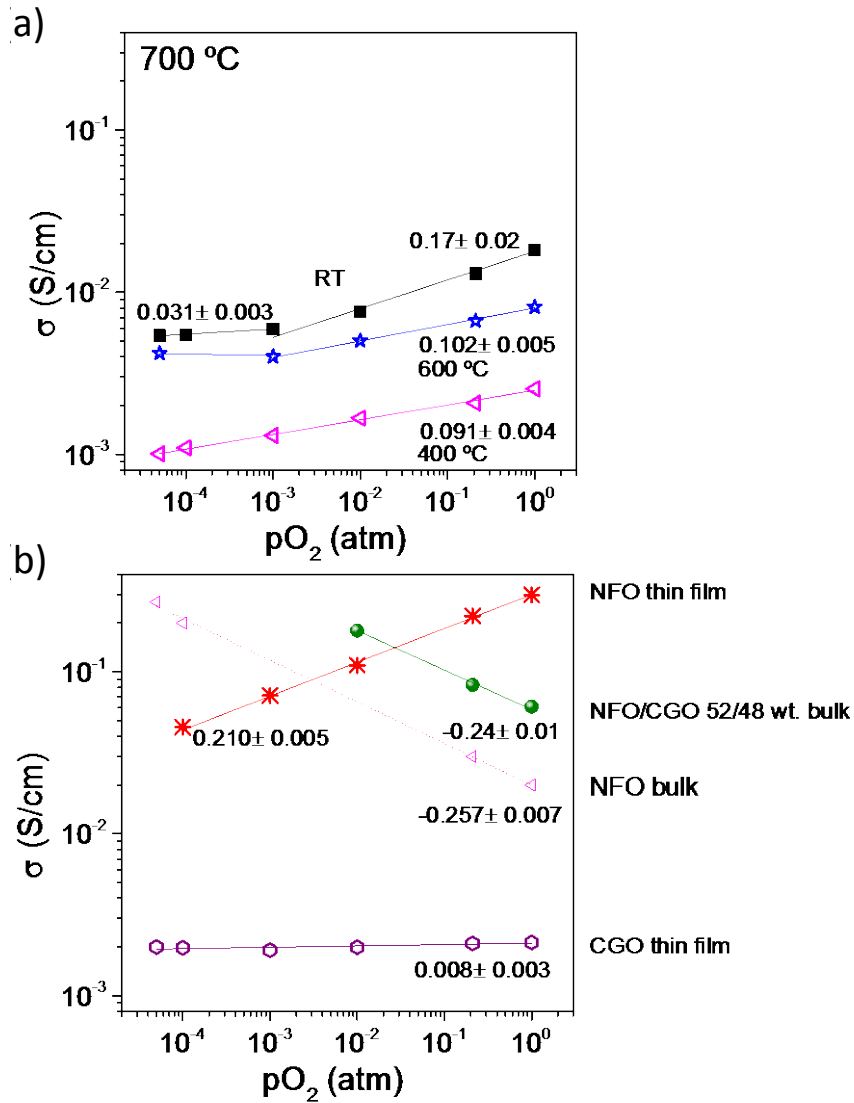
Figure 7: Total conductivity at 700 ºC as a function of pO_2 (a) of different cercer thin films and (b) of reference CGO and NFO thin films. Data of the NFO/CGO 52/48 bulk material is also plotted for comparison in both graphs. Thin films annealed at 800ºC. r.f. 25/25 W.

In order to study the change of ambipolar conductivity of the deposited films with the NFO/CGO ratio, the sputtering conditions were varied. The content of CGO was decreased by reducing the applied power to the CGO target during the deposition and leaving constant the NFO applied power (25 W). The composite film obtained when 25 W are applied to CGO gives rise to a NFO/CGO ~ 1/6 (wt/wt) while this ratio changes to ~ 2/1 (wt/wt) when applying 8W to the CGO target (XPS spectrum and SEM microstructure of this thin film in Supplementary information Figure S5). Figure 9 presents the total conductivity as a

function of the pO_2 for two composites films deposited at 400 ºC and annealed at 800 ºC. The conduction character of the thin film is determined by the prevailing crystalline phase, in line with a simple additive behavior of conduction properties. Namely, the higher the amount of NFO phase, the higher the total conductivity (quite close to the values of the NFO film) and it is obtained the same ¼ slope characteristic of a predominant p-type electronic conductor. Accordingly, the higher the amount of CGO, the lower the total conductivity, with values similar to those of the CGO film but with a slight dependence on the pO_2. This dependence can be assigned to the electronic conductivity through the NFO electronic conducting pathways, and the smaller values at very low pO_2 can be attributed to three aspects: (i) p-type electronic character of sputtered NFO particles; (ii) the lower vol. fraction of ionic-phase; and also possibly (iii) limitations in the percolation among CGO grains (ionic pathways). Therefore, composite thin-film layers produced by applying a NFO/CGO r.f. power of 25/8 W resulted in the highest total conductivity for a NFO/CGO ratio of 2/1.
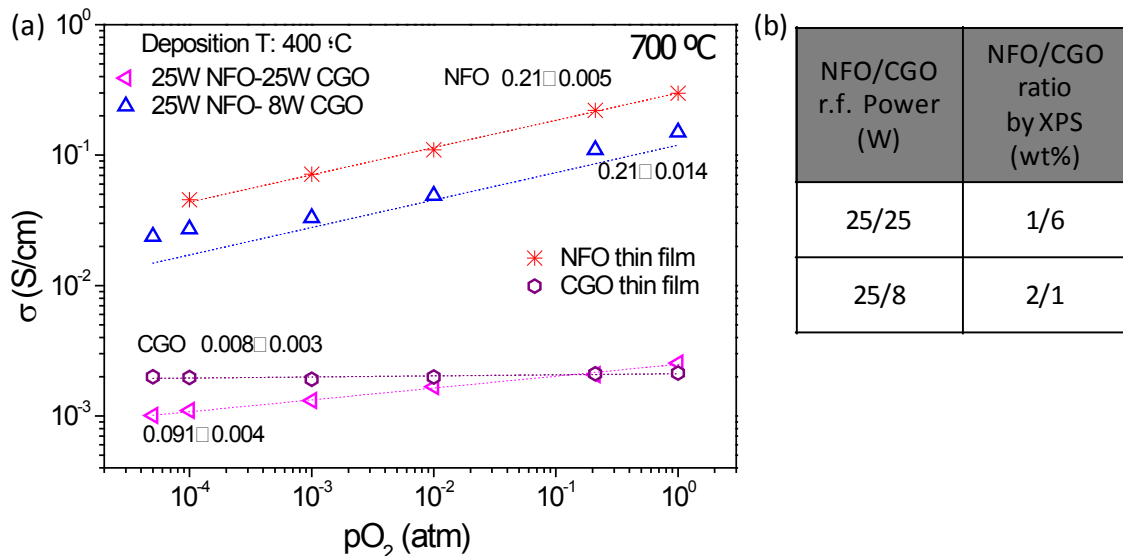

Figure 8: Total conductivity at 700ºC as a function of the pO_2 of NFO/CGO composites films with different NFO/CGO ratios and reference NFO and CGO films, all deposited at 400 ºC (a) and NFO/CGO ratios measured by XPS (b).

Conductivity relaxation profiles at 750 ºC upon oxidation and reduction, i.e. step-change from air to pure oxygen and *vice versa*, are depicted in Figure 5 for NFO/CGO (1/6) and NFO thin films. Note that the relaxation curve of a CGO thin film in this range of pO_2

cannot be measured, as there is no change in conductivity in this range of pO_2. The relaxation process of the nanocomposite thin film is much faster than that of pure NFO thin film. As we are measuring thin films this can only be ascribed to faster surface exchange kinetics of the nanocomposite. By fitting the curves to equation 1, surface reaction, k coefficients of $2.3x10^{-7}$ and $8.7x10^{-8}$ cm/s were obtained for oxidation and reduction of the nanocomposite film whereas k values $1.8x10^{-8}$ and $1.5x10^{-8}$ cm/s were measured for oxidation and reduction of the NFO film.[25] Surface exchange is boosted by one order of magnitude faster by providing oxygen-ion conduction to the NFO film, i.e, by creating a highly-packed nanocomposite with CGO ionic phase. This phenomena has been previously observed for bulk NFO/CGO composites as inferred from pulse O^{16}/O^{18} isotopic exchange measurements. The k values of the composite thin film are in the same order of magnitude as those reported for $Ce_{0.69}Gd_{0.31}O_{2-\delta}$ single crystals ($k = 4x10^{-8}$ cm/s at 750 ºC) while a huge increase of this kinetic parameter is expected if electronic conductivity is promoted in the doped-ceria matrix.[8b, 31]
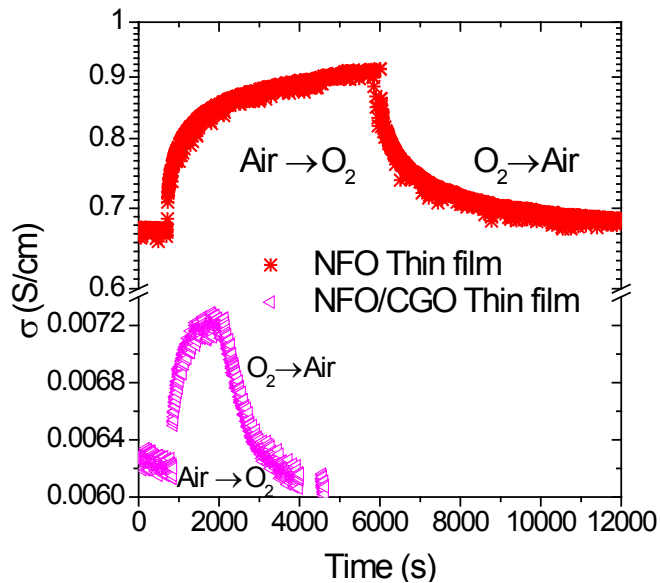

Figure 9: Conductivity relaxation curves at 750 ºC of a NFO/CGO composite thin film (a) and a NFO thin film (b)

Aiming to check NFO/CGO nanocomposite thin film suitability for oxyfuel applications, the stability of both phases in the sample deposited at 400ºC with an annealing at 800ºC

was checked at 750ºC for 48h in an atmosphere containing 250 ppm of SO_2, 5% of O_2, 3% H_2O and balanced with CO_2. XRD analysis are performed before and after treatment to confirm the absence of changes in the phase caused by SO_2, H_2O or CO_2. Figure 10 shows XRD patterns of the sample before and after the stabilization treatment where there are no changes in the phase before the treatment. Thus, the composite thin film appears to be stable under highly-demanding oxyfuel conditions where SO_2, H_2O or CO_2 are present.
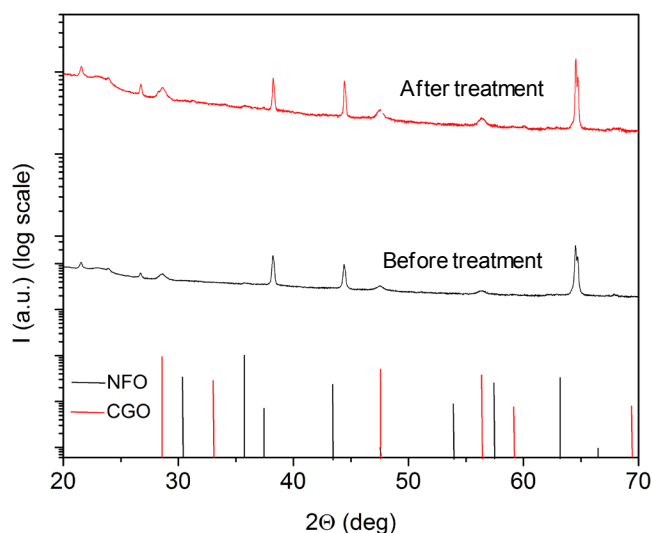

Figure 10: XRD patterns of NFO/CGO composite film deposited at 400ºC after annealing at 800ºC before and after stability treatment at 750ºC for 48h in an atmosphere containing 250 ppm of SO_2, 5% of O_2, 3% H_2O and balanced with CO_2. NFO and CGO reference patterns are also showed.

Finally, the application of NFO/CGO thin film layers as oxygen transport membranes was studied by conducting O_2 permeation tests. A 150 nm-thick NFO/CGO layer was deposited on top of a BSCF asymmetric membrane (20 μm-thick dense layer on a porous support, see cross-section Figure 12a). Nanocomposite layers were deposited by applying an r.f. power of 25/8 W on the NFO/CGO target at 400 ºC. NFO/CGO deposition on BSCF was selected to combine both high permeation features of BSCF membranes [16] and good stability of NFO/CGO under oxyfuel environments [9d, 10, 32]. Accordingly, the oxygen permeation was studied at different temperatures (1000 - 900 ºC) and varying the CO_2 content in the sweep stream.

O$_2$ fluxes $J(O_2)$ through the non-coated BSCF membrane suffer an important decay (Figure 11) when increasing CO$_2$ concentration in the sweep that becomes more significant at lower temperatures. Under pure CO$_2$ sweeping, the uncoated BSCF membrane exhibits $J(O_2)$ of 0.66, 0.29 and 0.12 ml·min^{-1}·cm^{-2} at 1000, 950 and 900 ºC, respectively, whereas under pure Ar sweeping O$_2$ fluxes are in the range of 10-7.4 ml·min^{-1}·cm^{-2}. When the NFO/CGO layer is deposited on the BSCF membrane surface, the resulting membrane assembly still delivers high $J(O_2)$ under clean conditions, thus proving both the proper ambipolar conduction and high surface exchange activity of the nanocomposite sputtered layer. Furthermore, the permeation decay of the membrane subjected to CO$_2$ environments is significantly lower than for the non-coated membrane. (Figure 11, note the log scale in y-axis) Under full CO$_2$ sweeping conditions, $J(O_2)$ values of 3.8, 1.3 and 0.4 ml·min^{-1}·cm^{-2} at 1000, 950 and 900 ºC are obtained, respectively. In a similar study performed on a screen-printed 10 μm-thick NiFe$_2$O-Ce$_{0.8}$Tb$_{0.2}$O$_{2-\delta}$ (NFO/CTO) membrane on a porous La$_{0.6}$Sr$_{0.4}$Co$_{0.2}$Fe$_{0.8}$O$_{3-\delta}$ support, [15] the $J(O_2)$ at 1000 ºC through the membrane improved with regard to Ar sweeping. Better sweeping properties are observed for CO$_2$ at very high temperatures while the CO$_2$ higher thermal emissivity enables to increase temperature on membrane surface and subsequently the O$_2$ fluxes. [9d, 33] Contrarily, the permeation of the NFO/CGO sputtered layer decreases when exposed to such environments at 1000-900 ºC. The latter was previously observed by Luo et al., [7, 10] and can be ascribed to O$_2$/CO$_2$ competitive adsorption processes inhibiting oxygen reactions on the surface active sites. [7, 9d, 10, 33] Besides, a slight degradation can be identified in the nano-grained NFO/CGO layer after testing and thermal cycling (1040 ºC to 700ºC) (Figure S6) and this may contribute to this loss in performance. Initially, and as can be seen in Figure 12b, a dense 150 μm-thick NFO/CGO layer is deposited uniformly on top of BSCF surface, covering completely BSCF membrane surface (Figures 12c and d). After the thermal cycling resulting from characterization (Figure S7), the NFO/CGO layer partially detached or disappeared in some particular areas. Therefore, the interaction of BSCF membrane in direct contact with CO$_2$ subsequently produced a loss in permeation, indicating that the robustness of the 150 nm-thick layer is not sufficient for operation at 1000 ºC. Further work for the optimization of the layer needs to be done in terms of thickness and uniformity while the optimal operation regime should be identified, typically below 900 ºC.

According to the obtained permeation results, a good performance is observed for NFO/CGO nanocomposite layers when working as OTM under oxyfuel conditions, delivering high oxygen permeation values even when exposed to full CO_2 environments. Additionally, the use of NFO/CGO nanocomposite layers obtained by r.f. magnetron co-sputtering could be also considered for the protection of highly permeating materials like BSCF in applications where stability in harsh gas environments is indispensable.
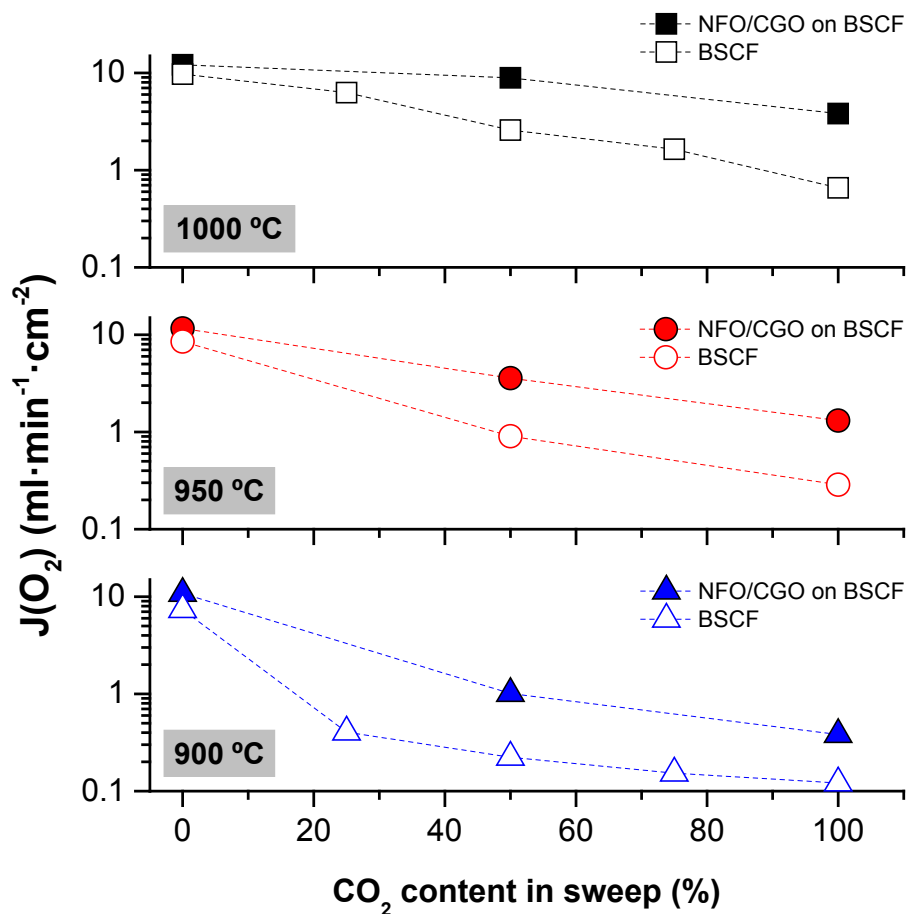

Figure 11: Permeation results of the bare and co-sputtered membrane as a function of testing temperature and CO_2 concentration in the sweep gas. (Experimental conditions: 300 ml·min⁻¹ air feeding, 300 ml·min⁻¹ Ar/CO_2 mixtures sweeping)
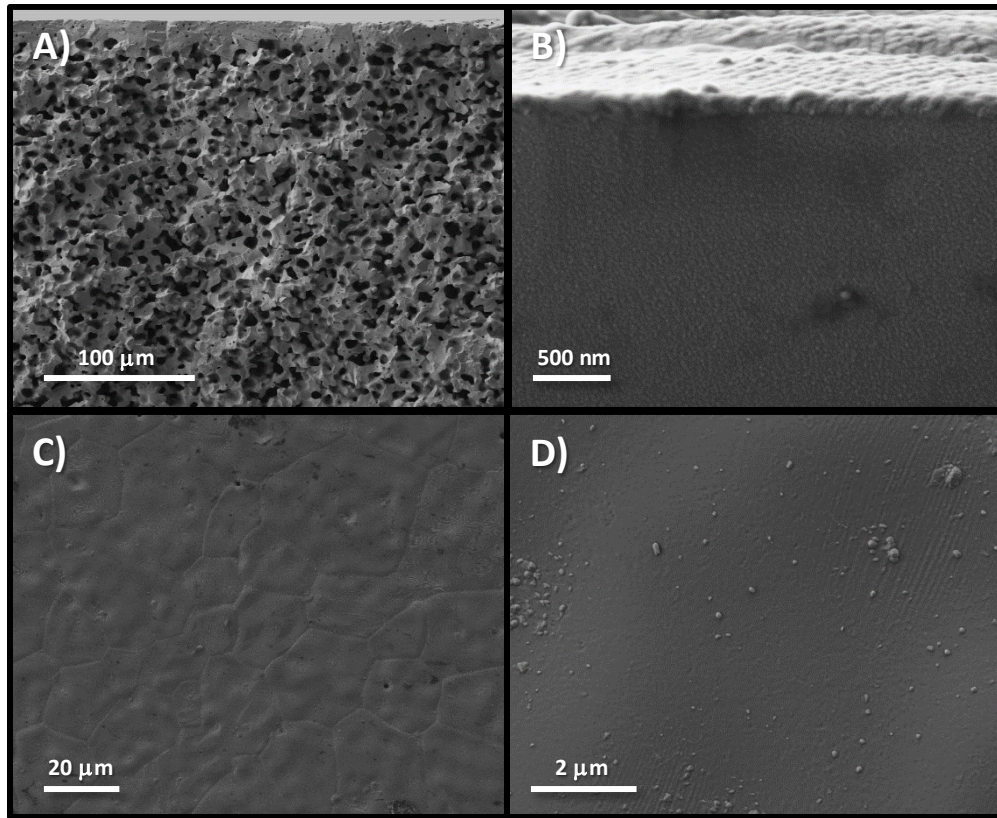
Figure 12: FESEM images of NFO/CGO layer deposited on a supported all-BSCF membrane: cross-section views (a) and (b), surface views (c) and (d).

4. Summary and conclusions

NiFe$_2$O$_4$ - Ce$_{0.8}$Gd$_{0.2}$O$_{2-\delta}$ (NFO – CGO) nanocomposite thin films were prepared by r.f. magnetron co-sputtering of individual NFO and CGO ceramic targets and optimized as a function of deposition temperature. The best microstructure and conduction properties were obtained for the film deposited at 400 ºC. The total transport properties, studied by total conductivity measurements as a function of the temperature and the pO$_2$, showed mixed electronic-ionic conduction due to the presence of the two highly-packed nano-grained phases, i.e., NFO electronic conducting phase and the CGO ionic phase. The p-type electronic behavior was correlated with the hole hopping between Ni^{3+} - Ni^{2+} (oxidation states of Ni measured by XPS) previously showed in the NFO thin films. The ratio of both phases was changed by applying different power to the ceramic targets and the expected amount of each deposited phase was measured by XPS. Furthermore, by changing ratio

between NFO and CGO in the deposition process, the thin films exhibited preferential ionic or electronic conductivity. Finally, the use of NFO/CGO thin films as oxygen transport membranes was studied by coating an asymmetric BSCF membrane. The resulting membrane assembly showed a remarkably better oxygen permeation performance in operation under CO_2-rich gas environments. Specifically, an improvement up to 3-5-fold rise in the fluxes was achieved under pure CO_2 atmosphere, with a peak flux of 3.8 ml·min^{-1}·cm^{-2} at 1000 ºC.

References

[1]   N. MacDowell, N. Florin, A. Buchard, J. Hallett, A. Galindo, G. Jackson, C. S. Adjiman, C. K. Williams, N. Shah, P. Fennell, *Energy & Environmental Science* **2010**, *3*, 1645-1669.

[2]   M. J. den Exter, W. G. Haije, J. F. Vente, in *Inorganic Membranes for Energy and Environmental Applications* (Ed.: A. Bose), Springer New York, **2009**, pp. 27-51.

[3]   aM. A. Habib, H. M. Badr, S. F. Ahmed, R. Ben-Mansour, K. Mezghani, S. Imashuku, G. J. la O, Y. Shao-Horn, N. D. Mancini, A. Mitsos, P. Kirchen, A. F. Ghoneim, *International Journal of Energy Research* **2011**, *35*, 741-764; bS. S. Hashim, A. R. Mohamed, S. Bhatia, *Renewable & Sustainable Energy Reviews* **2011**, *15*, 1284-1293; cP. Markewitz, J. Marx, A. Schreiber, P. Zapp, *Ghgt-11* **2013**, *37*, 2864-2876.

[4]   S. P. S. Badwal, F. T. Ciacchi, *Advanced Materials* **2001**, *13*, 993-+.

[5]   U. Nigge, H. D. Wiemhöfer, E. W. J. Römer, H. J. M. Bouwmeester, T. R. Schulte, *Solid State Ionics* **2002**, *146*, 163-174.

[6]   aA. L. Shaula, V. V. Kharton, F. M. B. Marques, A. V. Kovalevsky, A. P. Viskup, E. N. Naumovich, *J. Solid State Electrochem.* **2006**, *10*, 28-40; bF. Liang, H. Luo, K. Partovi, O. Ravkina, Z. Cao, Y. Liu, J. Caro, *Chemical Communications* **2014**, *50*, 2451-2454; cU. Pippardt, J. Boer, C. Bollert, A. Hoffmann, M. Heidenreich, R. Kriegel, M. Schulz, A. Simon, *Journal of Ceramic Science and Technology* **2014**, *5*, 309-316; dJ. Kniep, Q. Yin, I. Kumakiri, Y. S. Lin, *Solid State Ionics* **2010**, *180*, 1633-1639; eW. Fang, F. Liang, Z. Cao, F. Steinbach, A. Feldhoff, *Angewandte Chemie-International Edition* **2015**, *54*, 4847-4850; fS. Pirou, J. Gurauskis, V. Gil,

M. Sogaard, P. V. Hendriksen, A. Kaiser, S. Ovtar, R. Kiebach, *Fuel Processing Technology* **2016**, *152*, 192-199.

[7]   H. Luo, H. Jiang, K. Efimov, J. Caro, H. Wang, *AIChE J.* **2011**, *57*, 2738-2745.

[8]   aM. Balaguer, C. Solis, J. M. Serra, *Journal of Physical Chemistry C* **2012**, *116*, 7975-7982; bM. Balaguer, C. Solis, J. M. Serra, *Chemistry of Materials* **2011**, *23*, 2333-2343; cJ. Yi, Y. Zuo, W. Liu, L. Winnubst, C. Chen, *J. Membr. Sci.* **2006**, *280*, 849-855.

[9]   aH. Takamura, K. Okumura, Y. Koshino, A. Kamegawa, M. Okada, *J. Electroceram.* **2004**, *13*, 613-618; bH. Takamura, H. Sugai, M. Watanabe, T. Kasahara, A. Kamegawa, M. Okada, *J. Electroceram.* **2006**, *17*, 741-748; cH. Luo, H. Jiang, K. Efimov, F. Liang, H. Wang, J. Caro, *Ind. Eng. Chem. Res.* **2011**, *50*, 13508-13517; dM. Balaguer, J. Garcia-Fayos, C. Solis, J. M. Serra, *Chemistry of Materials* **2013**, *25*, 4986-4993.

[10] H. Luo, K. Efimov, H. Jiang, A. Feldhoff, H. Wang, J. Caro, *Angewandte Chemie International Edition* **2011**, *50*, 759-763.

[11] Y. Rao, Z. Wang, L. Chen, R. Wu, R. Peng, Y. Lu, *International Journal of Hydrogen Energy* **2013**, *38*, 14329-14336.

[12] V. V. Kharton, A. V. Kovalevsky, A. P. Viskup, A. L. Shaula, F. M. Figueiredo, E. N. Naumovich, F. M. B. Marques, *Solid State Ionics* **2003**, *160*, 247-258.

[13] B. C. H. Steele, *Current Opinion in Solid State and Materials Science* **1996**, *1*, 684-691.

[14] J. Sunarso, S. Baumann, J. M. Serra, W. A. Meulenberg, S. Liu, Y. S. Lin, J. C. D. da Costa, *Journal of Membrane Science* **2008**, *320*, 13-41.

[15] C. Gaudillere, J. Garcia-Fayos, M. Balaguer, J. M. Serra, *Chemsuschem* **2014**, *7*, 2554-2561.

[16] S. Baumann, J. M. Serra, M. P. Lobera, S. Escolástico, F. Schulze-Küppers, W. A. Meulenberg, *Journal of membrane Science* **2011**, *377*, 198-205.

[17] I. Garcia-Torregrosa, M. P. Lobera, C. Solis, P. Atienzar, J. M. Serra, *Advanced Energy Materials* **2011**, *1*, 618-625.

[18] C. Solís, S. Somacescu, E. Palafox, M. Balaguer, J. M. Serra, *The Journal of Physical Chemistry C* **2014**, *118*, 24266-24273.

[19] Y. Xi, K. Gao, X. Pang, H. Yang, X. Xiong, H. Li, A. A. Volinsky, *Ceramics International* **2017**, *43*, 11992-11997.

[20] G. Liu, Y. Yang, B. Huang, X. Luo, S. Ouyang, G. Zhao, N. Jin, P. Li, *Applied Surface Science* **2016**, *370*, 53-58.

[21] H. Guo, Y. Li, X. Fang, K. Zhang, J. Ding, N. Yuan, *Materials Letters* **2016**, *162*, 97-100.

[22] aJ. Xiong, M. Z. Ghori, B. Henkel, T. Strunskus, U. Schürmann, L. Kienle, F. Faupel, *Acta Materialia* **2014**, *74*, 1-8; bJ. Xiong, M. Z. Ghori, B. Henkel, T. Strunskus, U. Schürmann, M. Deng, L. Kienle, F. Faupel, *Applied Physics A: Materials Science and Processing* **2017**, *123*.

[23] M. Yashima, T. Takizawa, *The Journal of Physical Chemistry C* **2010**, *114*, 2385-2392.

[24] M. Ruf, C. Solis, S. Escolastico, R. Dittmeyer, J. M. Serra, *Journal of Materials Chemistry A* **2014**, *2*, 18539-18546.

[25] G. Garcia, M. Burriel, N. Bonanos, J. Santiso, *Journal of The Electrochemical Society* **2008**, *155*, P28-P32.

[26] B. Baruwati, K. M. Reddy, S. V. Manorama, R. K. Singh, O. Parkash, *Applied Physics Letters* **2004**, *85*, 2833-2835.

[27] aM. Mogensen, N. M. Sammes, G. A. Tompsett, *Solid State Ionics* **2000**, *129*, 63-94; bW. C. Oliver, G. M. Pharr, *Journal of Materials Research* **1992**, *7*, 1564-1583; cQ. Fang, J. Y. Zhang, *Surface & Coatings Technology* **2002**, *151*, 100-104; dE. Jud, C. B. Huwiler, L. J. Gauckler, *Journal of the Ceramic Society of Japan* **2006**, *114*, 963-969; eY. J. Kim, Y. Gao, G. S. Herman, S. Thevuthasan, W. Jiang, D. E. McCready, S. A. Chambers, *Journal of Vacuum Science & Technology A* **1999**, *17*, 926-935; fA. Rothschild, W. Menesklou, H. L. Tuller, E. Ivers-Tiffee, *Chemistry of Materials* **2006**, *18*, 3651-3659; gC. Kleinlogel, L. J. Gauckler, *Solid State Ionics* **2000**, *135*, 567-573; hA. Kossoy, Y. Feldman, E. Wachtel, I. Lubomirsky, J. Maier, *Advanced Functional Materials* **2007**, *17*, 2393-2398; iI. Lubomirsky, *Solid State Ionics* **2006**, *177*, 1639-1642; jN. I. Karageorgakis, A. Heel, J. L. M. Rupp, M. H. Aguirre, T. Graule, L. J. Gauckler, *Advanced Functional Materials* **2011**, *21*, 532-539.

[28] aK. Masek, M. Vaclavu, P. Babor, V. Matolin, *Applied Surface Science* **2009**, *255*, 6656-6660; bR. Pascu, S. Somacescu, G. Epurescu, M. Filipescu, C. Luculescu, D. Colceag, P. Osiceanu, R. Birjega, B. Mitu, *Thin Solid Films* **2014**, *553*, 98-103.

[29] D. R. Baer, M. H. Engelhard, A. S. Lea, P. Nachimuthu, T. C. Droubay, J. Kim, B. Lee, C. Mathews, R. L. Opila, L. V. Saraf, W. F. Stickle, R. M. Wallace, B. S. Wright, *Journal of Vacuum Science & Technology A* **2010**, *28*, 1060-1072.

[30] aB. Baruwati, R. K. Rana, S. V. Manorama, *Journal of Applied Physics* **2007**, *101*, 014302-014307; bN. Ponpandian, P. Balaya, A. Narayanasamy, *Journal of Physics-Condensed Matter* **2002**, *14*, 3221-3237.

[31] E. Ruiz-Trejo, J. D. Sirman, Y. M. Baikov, J. A. Kilner, *Solid State Ionics* **1998**, *113–115*, 565-569.

[32] M. Balaguer, PhD thesis, Universitat Politècnica de València **2013**.

[33] aJ. Garcia-Fayos, M. Balaguer, J. M. Serra, *ChemSusChem* **2015**, *8*, 4242-4249; bJ. M. Serra, J. Garcia-Fayos, S. Baumann, F. Schulze-Kueppers, W. A. Meulenberg, *Journal of Membrane Science* **2013**, *447*, 297-305.

[34] J. M. Serra, J. Garcia-Fayos, S. Baumann, F. Schulze-Küppers, W. A. Meulenberg, *Journal of Membrane Science* **2013**, *447*, 297-305.